CARBON 93 (2015) 458–464

Available at www.sciencedirect.com

ScienceDirect

journal homepage: www.elsevier.com/locate/carbon

Confinement effects in irradiation of nanocrystalline diamond

Felipe Valencia [a,b], José D. Mella [a,b], Rafael I. González [a,b], Miguel Kiwi [a,b,*], Eduardo M. Bringa [c,d]

[a] Departamento de Física, Facultad de Ciencias, Universidad de Chile, Casilla 653, Santiago 7800024, Chile
[b] Centro para el Desarrollo de la Nanociencia y la Nanotecnología, CEDENNA, Avda. Ecuador 3493, Santiago 9170124, Chile
[c] CONICET, Argentina
[d] Facultad de Ciencias Exactas y Naturales, Universidad Nacional de Cuyo, Mendoza 5500, Argentina

ARTICLE INFO

Article history:
Received 10 March 2015
Accepted 18 May 2015
Available online 23 May 2015

ABSTRACT

Swift heavy ion irradiation does not generate amorphous tracks in diamond, contrary to what happens in graphite or in diamond-like carbon. Since nanocrystalline diamond is of interest for several technological applications we investigate the reason for this difference, by means of large scale atomistic simulations of ion tracks in nanocrystalline diamond, using a thermal spike model, with up to 2.5 million atoms, and grain sizes in the range 5–10 nm. We conclude that tracking can be achieved under these conditions, when it is absent in single crystal diamond: for 5 nm samples the tracking threshold is below 15 keV/nm. Point defects are observed below this threshold. As the energy loss increases the track region becomes amorphous, and graphitic-like, with predominant sp^2 hybridization. This higher sensitivity to irradiation can be related to a very large decrease in thermal conductivity of nanocrystalline diamond, due to grain boundary confinement of the heat spike which enhances localized heating of the lattice.

1. Introduction

The understanding of the response of materials to all sorts of irradiation has been a subject of interest for a long time. The energy transferred to electrons and nuclei is a key element to predict the way solids respond to irradiation. In particular, carbon-related materials offer a large variety of possible technological applications [1,2], from electrochemical storage [3] to field emission devices [4], biosensors [5] and gene delivery [6].

There is a need to develop techniques to modify the properties of diamond-related materials [7,8]. One possible way to do it, in a controlled fashion, is the use of ion irradiation [9,10]. In particular, fast ions used in Swift heavy ion (SHI) bombardment of a solid transfer energy to electronic excitations which in turn couple to the lattice, and lead to permanent modifications of the material along the ion path [11], in addition to surface effects like cratering [12] and sputtering [13].

Depending on the amount of energy deposited, determined by the electronic stopping power S_e, ion tracks can consist of isolated defects or a roughly cylindrical region of transformed material. For instance, SHI creates amorphous tracks in quartz [14], and significant defects in graphite [15,16], and diamond-like carbon (dlc) [17]. However, SHI bombardment of diamond only leads to some isolated defects,

* *Corresponding author at:* Departamento de Física, Facultad de Ciencias, Universidad de Chile, Casilla 653, Santiago 7800024, Chile.
E-mail address: m.kiwi.t@gmail.com (M. Kiwi).
http://dx.doi.org/10.1016/j.carbon.2015.05.067
0008-6223/

probably due to nuclear stopping [18]. The largest stopping power that has been measured was in diamond irradiation experiments, with 1 GeV uranium bombardment [19], and amounts to around 48 keV/nm. We notice that surface craters in diamond have been created by highly charged ion bombardment, which also leads to extremely localized electronic excitations [20].

Molecular dynamics (MD) simulations, using a cylindrical thermal spike model, showed that it might be possible to amorphize diamond, but only for extremely high energy depositions (larger than 50 keV/nm) if one assumes an efficiency of 0.2 for the effective stopping power [21]. This efficiency provides the fraction of the experimental stopping power which is transferred to the lattice, and contributes to track formation. Recent simulations using a two-temperature model [22] showed that stopping powers between 3 and 9 keV/nm lead only to some lattice strain, with point defects starting to form at 13 keV/nm. Experiments and simulations for dlc showed that the amorphous sp^3 structure transformed into an amorphous sp^2 structure with lower density. Therefore, a significant expansion of the material leading to surface hillocks, with a height that increases with electronic stopping power [23]. The inelastic thermal spike model provides a good description of track sizes in dlc [17], assuming an electron–phonon mean free path of 0.9 nm.

Nanostructured materials display interesting behavior under irradiation [10]. In particular, nanocrystalline (NC) materials have been shown to exhibit increased radiation resistance both in the nuclear regime [24,25], and in the electronic regime [26]. However, the case of nano-diamond seems to behave in the opposite way, with enhanced radiation damage due to the NC nature of the samples.

While NC metal samples display a thermal conductivity which is only slightly smaller than their coarse-grained counterparts, NC diamond has a thermal conductivity which could become 10–100 times smaller in the NC as compared with the single crystal case. This has been shown both by experiments [27–29], and simulations [30]. The change in thermal conductivity can be interpreted as a result of Kapitza resistance from the grain boundaries (GBs), or simply as a decrease of the phonon mean free path due to confinement in the nanograins, with GBs acting as scattering walls.

2. Method

Our simulations of the above described phenomena were performed using the modified reactive bond order (REBO) potential [31] within the LAMMPS code [32]. Nanodiamond targets were created for 5 nm ($50a_0 \times 50a_0 \times 15a_0$), 7 nm ($70a_0 \times 70a_0 \times 21a_0$) and 10 nm ($100a_0 \times 100a_0 \times 30\,a_0$) grain size, where $a_0 = 3.57$ Åis the diamond lattice parameter. MD simulations of NC diamond samples have been carried out for grain sizes smaller than 5 nm to study their mechanical properties, using Voronoi tessellation as done by Bringa et al. [33]. Nanodiamond agregates with 4–5 nm grain size can be achieved by detonation [34]. Given that nanocrystals are typically far from equilibrium we carry out an extensive relaxation of the samples. Initially, grain boundary atoms which are too close to each other are removed, resulting in a density with more than 99.8% of the single crystal density. Next annealing at 1800 K is carried out during 10 ps, together with a zero pressure barostat, before taking the samples back to 10 K. This low temperature simplifies defect analysis, and the results were similar to some selected 300 K simulations. The SHI track is introduced using a thermal spike model [35], with the same parameters which were successful in reproducing dlc results [23]. There are several models which include electron–phonon coupling in metals [36], and insulators [37], but this basic model offers good agreement with experiments for a number of materials, having been used for silica [38] and forsterite [39], and with a slightly modified model [40] it was also used for MgO.

The initial track is a cylindrical region along the z axis, with a 2 nm radius. All atoms inside the region are given a temperature consistent with the desired effective stopping power, with a heating time of 100 fs. An adaptive time step is used during the simulation to ensure energy conservation after the spike heating, with a maximum step of 1 fs. The simulation box is surrounded, in the xy plane, by a thin Langevin thermostat kept at the initial temperature. Spike evolution is followed during 50 ps, which is enough to guarantee cooling of the central spike with the help of the thermal bath in the outer boundary. Simulations shown here are for a spike located within a [0 0 1] oriented grain. Locating the spike near GB junctions increases disorder.

The track temperature is directly related to the effective stopping power. We use temperatures of 5 000 K, 10 000 K, 12 500 K, 15 000 K, 17 500 K, and 22 500 K, which correspond to effective stopping power S_e of ~1.7, 3.4, 4.2, 5.0, 5.9, and 7.6 keV/nm, respectively. In order to relate this to the experimental S_e we can assume an efficiency of 0.2, which provides excellent agreement between simulations and dlc experiments, to obtain S_e values in the range 8.5–38 keV/nm, which can be achieved with single ion bombardment in current experimental facilities.

3. Results

The evolution of a given SHI track in nanodiamonds is represented in Fig. 1, for $S_e = 29.5$ keV/nm. The track is always confined within the original grain. In single crystal diamond a shock wave is formed and propagates outwards [21], but here the GBs dissipate an important fraction of the outgoing energy and defuse this shock wave. After 20 ps the latent track presents a well defined defect profile, which will not evolve further until the end of the simulation. There could always be some re-structuring of point defects for very long times, but to study that would require other simulation techniques.

Fig. 2 shows the final frame of our simulations, for an initial $d = 7$ nm grain size, and for different track temperatures. Lowest temperatures lead only to point defects and some strain in the diamond lattice, as already observed in single crystal diamond [21,22]. However, in the 25–30 keV/nm range an amorphous track is formed. This can be contrasted to the experimental single crystal diamond case, which does not show tracking even close to 50 keV/nm. We note that a complex track structure emerges, with an amorphous core

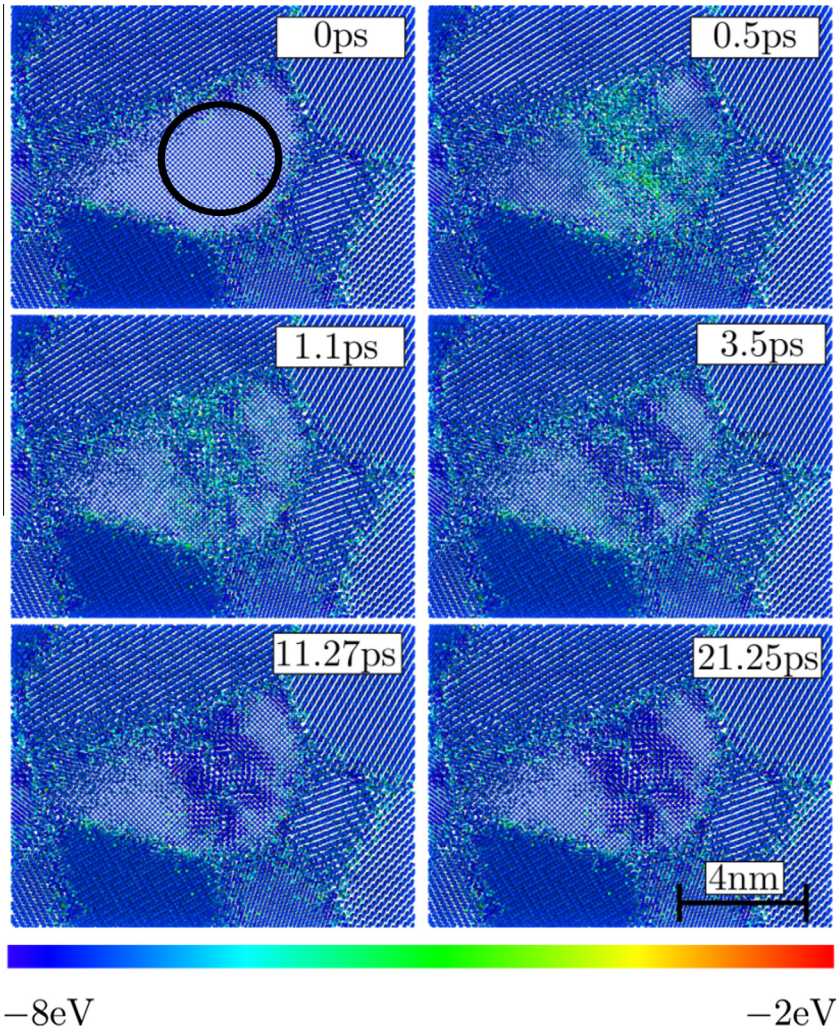

Fig. 1 – Time evolution of a thermal spike for $S_e = 29.5$ keV/nm at different times, for a 7 nm grain size. Atom colors represent the potential energy per atom, with grain boundaries displaying higher energy in comparison with atoms inside the grains. Notice the confinement of the track inside a single grain. The location of the initial track is denoted by the black circle in the 0 ps frame. (A colour version of this figure can be viewed online.)

surrounded by point defects. This structure with an inner track and a track halo has been observed in several experiments, for instance in amorphous silica tracks [37]. The exact location of the amorphization threshold might shift using other potentials like EDIP [41], but the general features are not expected to change.

The influence of grain size in the possible structural modifications of the sample are shown in Fig. 3, for an initial track of stopping power $S_e = 17$ keV/nm. In the 10 nm sample there are only a few point defects, while the 5 nm sample exhibits an amorphous track. The 7 nm sample displays an intermediate situation, with a small amorphous inner track and a halo of point defects.

In order to illustrate the role played by GBs on thermal conduction and confinement we show in Fig. 4a the radial temperature profiles at different times, for $d = 7$ nm and $S_e = 38$ keV/nm. Notice that the spike lasts for about 20 ps, in contrast to diamond simulations [21] where it lasts for just a few picoseconds. In addition, it is relevant to emphasize that the outer box boundary is not affected by the central heat pulse, indicating that the size of our samples is large enough to follow the spike. In the center of the track the differences are of the order of 1000 K. In Fig. 4b we observe that for radii larger than 4 nm the temperature profiles overlap, which constitutes an indication that heat propagation is faster in the large (10 nm) samples. This fact implies that grain size plays a key role in the phonon transport across the material.

SHI can create amorphous tracks with a lower density than the surrounding system (Fig. 5a), as it has been seen for tracks in amorphous silica [22,37]. Density profiles in our irradiated samples give track sizes in the 1–4 nm range, similar to the size range for tracks in dlc for equivalent stopping powers [23]. In the track core densities are consistent with graphitization and measurements for sp^2-bonded carbon [42,43], and other experimental papers reporting lower density for sp^2 carbon. Indeed, average atomic coordination of 3

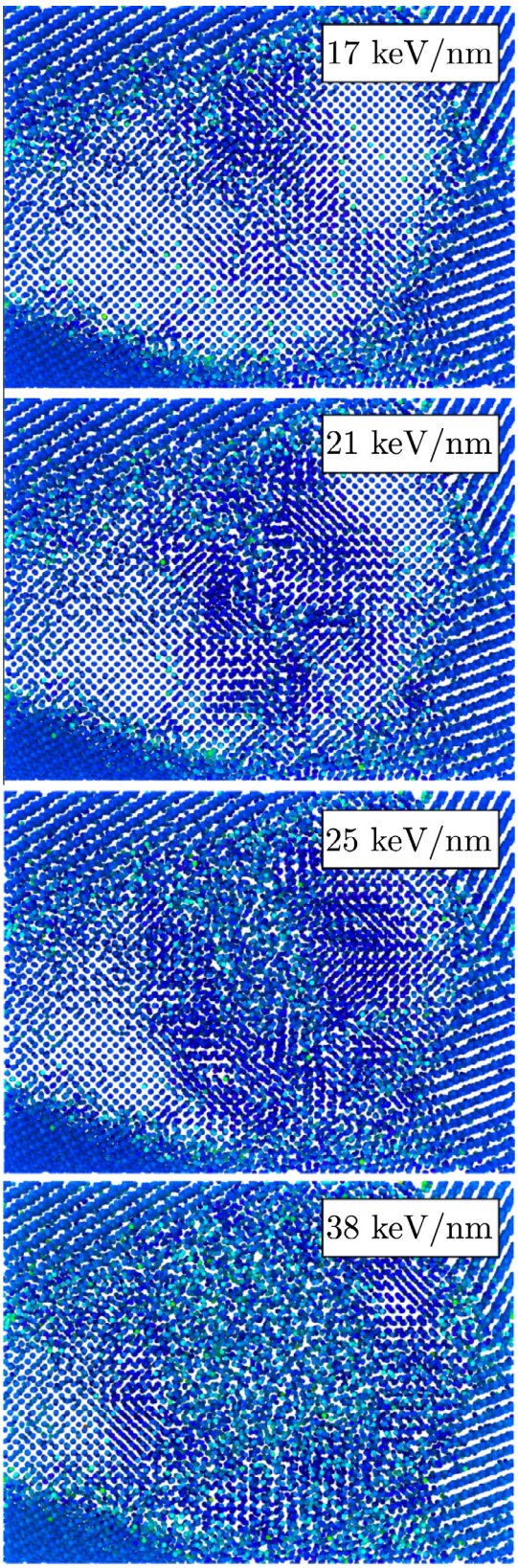

Fig. 2 – Track formation for different initial track temperatures, for 7 nm grain size, and $t = 20$ ps. Atom colors represent the potential energy per atom, with grain boundaries displaying larger energy in comparison with atoms inside the grains. (A colour version of this figure can be viewed online.)

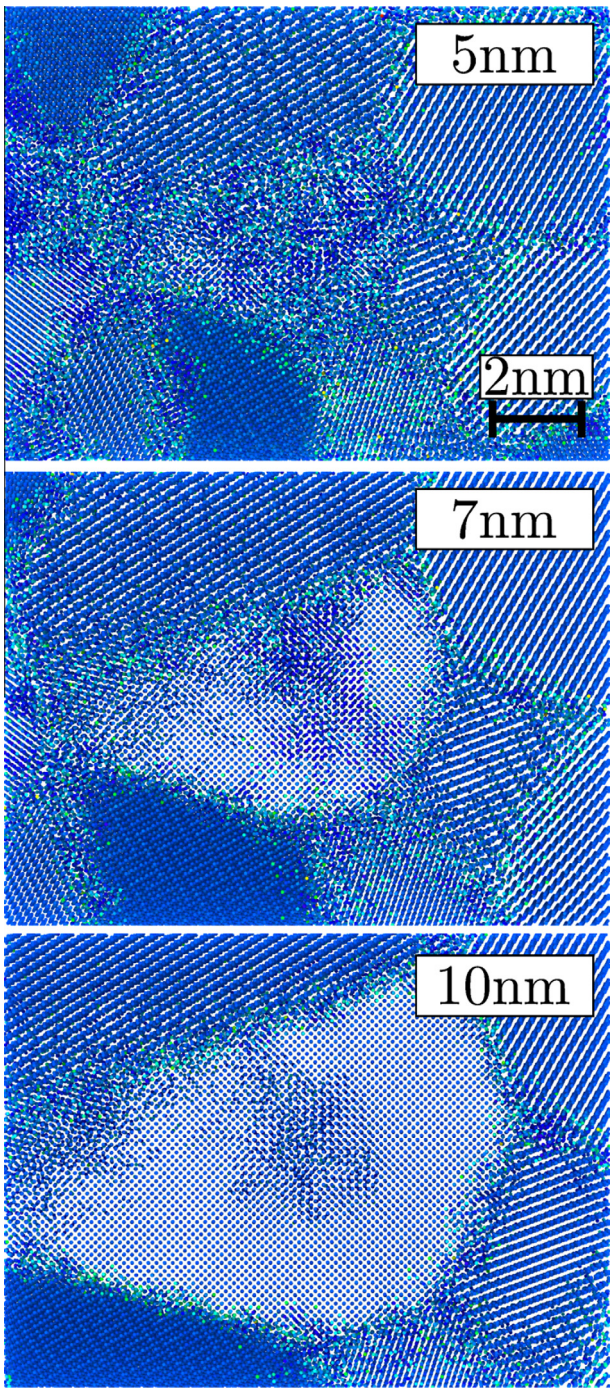

Fig. 3 – Effect of the thermal spike for different grain sizes, at the end of the simulation, for stopping power of $S_e = 17$ keV/nm. (A colour version of this figure can be viewed online.)

and 4 can be associated with sp^2 and sp^3 bonding, respectively, and the hybridization profiles in Fig. 5b show an sp^2 rich core. This sp^2 fraction increase is similar to what has been reported for tracks in dlc [23], and for cascade damage in tetrahedral amorphous carbon [44]. The presence of an amorphous track would affect the electrical conductivity of the sample, as in the case of amorphous pockets created by collision cascades in diamond [7].

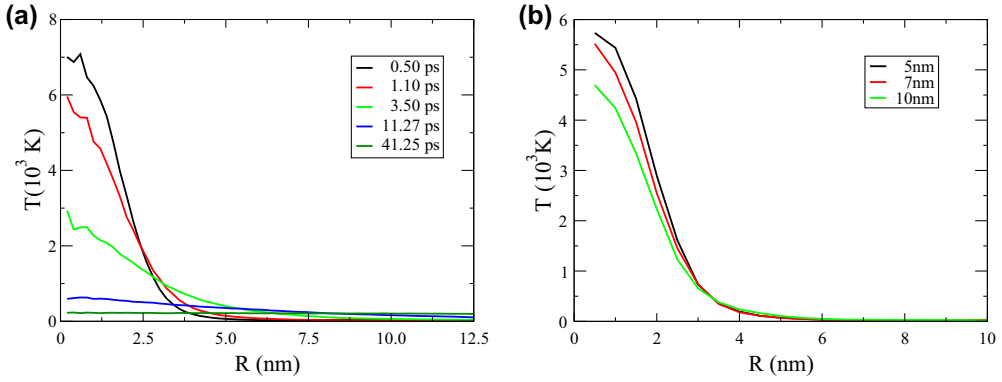

Fig. 4 – (a) Temperature profile at different times after a S_e = 4.2 keV/nm thermal spike, for a d = 7 nm grain size sample. The average was performed on cylindrical shells with 1 nm thickness whose axis coincides with the center of thermal spike. (b) Temperature profile at 0.6 ps for different grain sizes. (A colour version of this figure can be viewed online.)

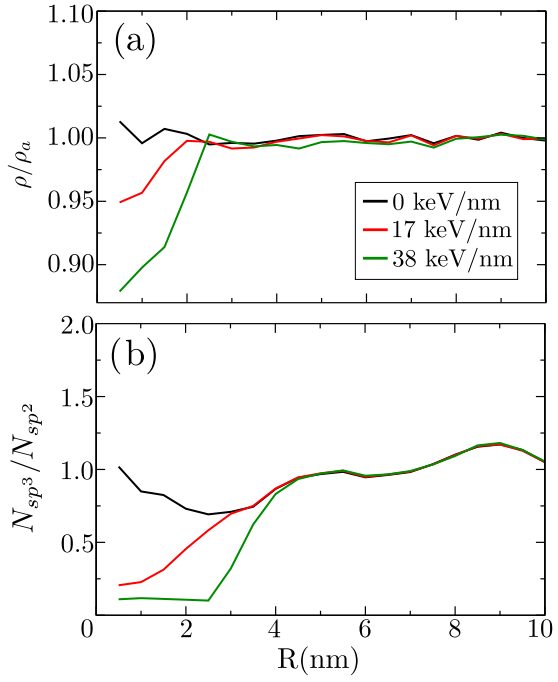

Fig. 5 – Analysis of the last MD simulation frame for d = 7 nm. Top: relative density. Bottom: sp^3/sp^2 fraction. ρ and ρ_a are the local and average densities, respectively. (A colour version of this figure can be viewed online.)

4. Summary and conclusions

Grain boundaries are typically assumed to reduce radiation effects [25,30], even in the electronic regime [26]. However, here we have shown an example where GBs enhance radiation effects in nanocrystalline C. Moreover, similar effects might be expected in other insulators with nanocrystalline structure.

In fact, single crystal diamond does not amorphize under SHI radiation until a stopping power $S_e \sim$50 keV/nm is reached, which is a difficult limit to attain using single SHI. However, we find that nanocrystalline diamond, with a size of ~5 nm, has an amorphization threshold of about 15 keV/nm, due to confinement effects of the track inside a nanograin. Similar to what has been observed in dlc [23], the material goes from sp^3 to sp^2 bonding, with a significant density decrease due to this coordination change. The phase change might display some level of reversibility, according to recent experiments on nanodiamond to nano-onions, to nanodiamond transformations [45], allowing the tuning of the degree of transformation of the materials by means of localized heating.

Up to this date we are not aware of any experiments on radiation damage on NC diamond. Transmission electron microscopy (TEM) studies would clearly reveal structural changes [46]. Given the change in hybridization, Raman spectroscopy [47,48] would provide an indirect measurement of track formation, provided that the ion fluence is large enough to result in a large track volume fraction. GB effects, in addition to nanograin effects, conspire to reduce the equilibrium heat conduction by more than one order of magnitude, compared to samples with micron-sized grains [30]. We notice that amorphous C conductivity decreases by 3 to 4 orders of magnitude with respect to diamond, and irradiated samples containing ion tracks would be much less conducting. Therefore, thermal conductivity measurements could also provide evidence of track formation.

Here we probed bulk effects, but surfaces might lead to additional features. For instance, carbon onions with high conductivity and surface area might be generated, as has been shown for nanodiamond clusters [49]. Conversion of sp^3 to sp^2 bonding might also lead to surface hillocks, as in dlc irradiation, providing nanostructured templates [23]. Future simulations will treat surface effects, including the possible role of H and other elements on the tracking threshold. Also, future studies could involve the use of reactive potentials, like ReaxFF [50,51] to include the possible effect of nitrogen vacancies during irradiation, given that they help tailoring nanocrystalline diamond for photonics and labeling applications [52,53].

Acknowledgments

EMB thanks useful comments by D. Schwen, P. Erhart, and K. Nordlund, and support from PICT-0092 and a SeCTyP-UNCuyo

grant. This work was supported by the Fondo Nacional de Investigaciones Científicas y Tecnológicas (FONDECYT, Chile) under grants #3140526 (RG), #1120399 and 1130272 (MK), and Financiamiento Basal para Centros Científicos y Tecnológicos de Excelencia FB-0807 (RG, FV, JM, and MK). FV was supported by CONICYT Doctoral Fellowship grant #21140948.

REFERENCES

[1] Cha C, Shin SR, Annabi N, Dokmeci MR, Khademhosseini A. Carbon-based nanomaterials: multifunctional materials for biomedical engineering. ACS Nano 2013;7(4):2891–7.
[2] Mochalin V, Shenderova O, Ho D, Gogotsi Y. The properties and applications of nanodiamonds. Nat Nanotech 2012;7(1):11–23.
[3] Gu W, Peters N, Yushin G. Functionalized carbon onions, detonation nanodiamond and mesoporous carbon as cathodes in Li-ion electrochemical energy storage devices. Carbon 2013;53(0):292–301.
[4] Okotrub A, Bulusheva L, Gusel'nikov A, Kuznetsov V, Butenko Y. Field emission from products of nanodiamond annealing. Carbon 2004;42(56):1099–102.
[5] Singh M, Holzinger M, Biloivan O, Cosnier S. 3D-nanostructured scaffold electrodes based on single-walled carbon nanotubes and nanodiamonds for high performance biosensors. Carbon 2013;61(0):349–56.
[6] Zhang X-Q, Chen M, Lam R, Xu X, Osawa E, Ho D. Polymer-functionalized nanodiamond platforms as vehicles for gene delivery. ACS Nano 2009;3(9):2609–16.
[7] Prawer S, Kalish R. Ion-beam-induced transformation of diamond. Phys Rev B 1995;51(22):15711.
[8] Hoffman A, Prawer S, Kalish R. Structural transformation of diamond induced by 1-keV Ar-ion irradiation as studied by Auger and secondary-electron spectroscopies and total-secondary-electron-yield measurements. Phys Rev B 1992;45(22):12736.
[9] Christie H, Robinson M, Roach D, Ross D, Suarez-Martinez I, Marks N. Simulating radiation damage cascades in graphite. Carbon 2015;81(0):105–14.
[10] Krasheninnikov A, Nordlund K. Ion and electron irradiation-induced effects in nanostructured materials. J Appl Phys 2010;107(7):071301.
[11] Toulemonde M, Trautmann C, Balanzat E, Hjort K, Weidinger A. Track formation and fabrication of nanostructures with MeV-ion beams. Nucl Instrum Methods Phys Res B 2004;216:1–8.
[12] Papaléo R, Leal R, Trautmann C, Bringa E. Cratering by MeV–GeV ions as a function of angle of incidence. Nucl Instrum Methods Phys Res B 2003;206:7–12.
[13] Bringa EM, Caro A, Wang Y, Victoria M, McNaney JM, Remington BA, et al. Ultrahigh strength in nanocrystalline materials under shock loading. Science 2005;309(5742):1838–41.
[14] Meftah A, Brisard F, Costantini JM, Dooryhee E, Hage-Ali M, Hervieu M, et al. Track formation in SiO_2 quartz and the thermal-spike mechanism. Phys Rev B 1994;49:12457–63.
[15] Liu J, Neumann R, Trautmann C, Müller C. Tracks of swift heavy ions in graphite studied by scanning tunneling microscopy. Phys Rev B 2001;64:184115.
[16] Zeng J, Yao H, Zhang S, Zhai P, Duan J, Sun Y, et al. Swift heavy ions induced irradiation effects in monolayer graphene and highly oriented pyrolytic graphite. Nucl Instrum Methods Phys Res B 2014;330:18–23.
[17] Rotaru C, Pawlak F, Khalfaoui N, Dufour C, Perrière J, Laurent A, et al. Track formation in two amorphous insulators, vitreous silica and diamond like carbon: experimental observations and description by the inelastic thermal spike model. Nucl Instrum Methods Phys Res B 2012;272:9–14.
[18] Krauser J, Zollondz J-H, Weidinger A, Trautmann C. Conductivity of nanometer-sized ion tracks in diamond-like carbon films. J Appl Phys 2003;94(3):1959–64.
[19] Ziegler J, Stopping and ranges in matter (SRIM), URL http://www.srim.org, 2009.
[20] Makgato T, Sideras-Haddad E, Shrivastava S, Schenkel T, Ritter R, Kowarik G, et al. Highly charged ion impact induced nanodefects in diamond. Nucl Instrum Methods Phys Res B 2013;314:135–9.
[21] Schwen D, Bringa E. Atomistic simulations of swift ion tracks in diamond and graphite. Nucl Instrum Methods Phys Res B 2007;256(1):187–92.
[22] Pakarinen OH, Djurabekova F, Nordlund K. Density evolution in formation of swift heavy ion tracks in insulators. Nucl Instrum Methods Phys Res B 2010;268(19):3163–6.
[23] Schwen D, Bringa E, Krauser J, Weidinger A, Trautmann C, Hofsäss H. Nano-hillock formation in diamond-like carbon induced by swift heavy projectiles in the electronic stopping regime: experiments and atomistic simulations. Appl Phys Lett 2012;101(11):113115.
[24] Samaras M, Derlet P, Van Swygenhoven H, Victoria M. Computer simulation of displacement cascades in Nanocrystalline Ni. Phys Rev Lett 2002;88:125505.
[25] Bai X-M, Voter AF, Hoagland RG, Nastasi M, Uberuaga BP. Efficient annealing of radiation damage near grain boundaries via interstitial emission. Science 2010;327(5973):1631–4.
[26] Chimi Y, Iwase A, Ishikawa N, Kobiyama M, Inami T, Okuda S. Accumulation and recovery of defects in ion-irradiated nanocrystalline gold. J Nucl Mater 2001;297(3):355–7.
[27] Kidalov S, Shakhov F, Vul A. Thermal conductivity of sintered nanodiamonds and microdiamonds. Diamond Relat Mater 2008;17(45):844–7.
[28] Kidalov S, Shakhov F, Vul A. Thermal conductivity of nanocomposites based on diamonds and nanodiamonds. Diamond Relat Mater 2007;16(12):2063–6.
[29] Balandin AA. Thermal properties of graphene and nanostructured carbon materials. Nat Mater 2011;10(8):569–81.
[30] Dong H, Wen B, Melnik R. Relative importance of grain boundaries and size effects in thermal conductivity of nanocrystalline materials. Sci Rep 2014;4:7037.
[31] Stuart SJ, Tutein AB, Harrison JA. A reactive potential for hydrocarbons with intermolecular interactions. J Chem Phys 2000;112(14):6472–86.
[32] Plimpton S. Fast parallel algorithms for short-range molecular dynamics. J Comput Phys 1995;117(1):1–19.
[33] Bringa EM, Caro A, Wang Y, Victoria M, McNaney JM, Remington BA, et al. Ultrahigh strength in nanocrystalline materials under shock loading. Science 2005;309(5742):1838–41.
[34] Krüger A, Kataoka F, Ozawa M, Fujino T, Suzuki Y, Aleksenskii A, et al. Unusually tight aggregation in detonation nanodiamond: Identification and disintegration. Carbon 2005;43(8):1722–30.
[35] Bringa EM, Johnson RE, Jakas M. Molecular-dynamics simulations of electronic sputtering. Phys Rev B 1999;60:15107–16.
[36] Duffy D, Rutherford A. Including the effects of electronic stopping and electron–ion interactions in radiation damage simulations. J Phys Condens Matter 2007;19(1):016207.

[37] Kluth P, Schnohr CS, Pakarinen OH, Djurabekova F, Sprouster DJ, Giulian R, et al. Fine structure in swift heavy ion tracks in amorphous SiO 2. Phys Rev Lett 2008;101(17):175503.
[38] Chun-E L, Jian-Ming X, Yu-Gang W, Yan-Wen Z. Molecular dynamics simulation of latent track formation in α-quartz. Chin Phys C 2013;37(3):038201.
[39] Devanathan R, Durham P, Du J, Corrales LR, Bringa EM. Molecular dynamics simulation of amorphization in forsterite by cosmic rays. Nucl Instrum Methods Phys Res B 2007;255(1):172–6.
[40] Scott C, Smith R, Sickafus K. Surface topography induced by swift heavy ion impacts. Nucl Instrum Methods Phys Res B 2011;269(14):1625–9.
[41] Marks NA. Generalizing the environment-dependent interaction potential for carbon. Phys Rev B 2000;63:035401.
[42] Haerle R, Riedo E, Pasquarello A, Baldereschi A. sp^2/sp^3 hybridization ratio in amorphous carbon from C 1s core-level shifts: X-ray photoelectron spectroscopy and first-principles calculation. Phys Rev B 2001;65:045101. http://dx.doi.org/10.1103/PhysRevB.65.045101. URL <http://link.aps.org/doi/10.1103/PhysRevB.65.045101>..
[43] Ferrari AC, Robertson J. Interpretation of Raman spectra of disordered and amorphous carbon. Phys Rev B 2000;61:14095–107. http://dx.doi.org/10.1103/PhysRevB.61.14095. URL <http://link.aps.org/doi/10.1103/PhysRevB.61.14095>..
[44] McCulloch DG, Gerstner EG, McKenzie DR, Prawer S, Kalish R. Ion implantation in tetrahedral amorphous carbon. Phys Rev B 1995;52:850–7. http://dx.doi.org/10.1103/PhysRevB.52.850. URL<http://link.aps.org/doi/10.1103/PhysRevB.52.850>..
[45] Xiao J, Ouyang G, Liu P, Wang CX, Yang GW. Reversible nanodiamond-carbon onion phase transformations. Nano Lett 2014;14(6):3645–52.
[46] Nian Q, Wang Y, Yang Y, Li J, Zhang MY, Shao J, et al. Direct laser writing of nanodiamond films from graphite under ambient conditions. Sci Rep 2014;4:6612.
[47] Ferrari AC, Robertson J. Raman spectroscopy of amorphous, nanostructured, diamond–like carbon, and nanodiamond. Philos Trans R Soc London Ser A 2004;362(1824):2477–512.
[48] Li W, Irle S, Witek H. Convergence in the evolution of nanodiamond raman spectra with particle size: A theoretical investigation. ACS Nano 2010;4(8):4475–86.
[49] Zeiger M, Jäckel N, Aslan M, Weingarth D, Presser V. Understanding structure and porosity of nanodiamond-derived carbon onions. Carbon 2015;84(0):584–98.
[50] Nielson KD, van Duin ACT, Oxgaard J, Deng W-Q, Goddard WA. Development of the ReaxFF reactive force field for describing transition metal catalyzed reactions, with application to the initial stages of the catalytic formation of carbon nanotubes. J Phys Chem A 2005;109(3):493–9.
[51] Kamat AM, van Duin ACT, Yakovlev A. Molecular dynamics simulations of laser-induced incandescence of soot using an extended ReaxFF reactive force field. J Phys Chem A 2010;114(48):12561–72.
[52] Chang Y-R, Lee H-Y, Chen K, Chang C-C, Tsai D-S, Fu C-C, et al. Mass production and dynamic imaging of fluorescent nanodiamonds. Nat Nanotech 2008;3(5):284–8.
[53] Tisler J, Balasubramanian G, Naydenov B, Kolesov R, Grotz B, Reuter R, et al. Fluorescence and spin properties of defects in single digit nanodiamonds. ACS Nano 2009;3(7):1959–65.